RSC Advances

PAPER

View Article Online
View Journal | View Issue

Open Access Article. Published on 24 August 2021. Downloaded on 1/2/2026 2:42:14 AM.
This article is licensed under a Creative Commons Attribution-NonCommercial 3.0 Unported Licence.

Check for updates

Cite this: *RSC Adv.*, 2021, **11**, 28496

Preparation of Mn_2O_3/MIL-100(Fe) composite and its mechanism for enhancing the photocatalytic removal of rhodamine B in water†

Nguyen Trung Dung,*[a] Tran Thi Hue,[a] Vu Dinh Thao[a] and Nguyen Nhat Huy *[bc]

Received 5th May 2021
Accepted 6th August 2021

DOI: 10.1039/d1ra03496k

rsc.li/rsc-advances

In this study, Mn_2O_3/MIL-100(Fe) composite was successfully synthesized by the hydrothermal method and applied for photocatalytic removal of rhodamine B (RhB) in water. The physical and chemical properties of the synthesized materials were characterized by XRD, FTIR, SEM, UV-visible, and BET analyses. Experimental results showed a great enhancement in the photocatalytic ability of the Mn_2O_3/MIL-100(Fe) composite as compared to individual Mn_2O_3 or MIL-100(Fe) under visible light and persulfate activation. The affecting factors such as pH, photocatalyst dose, RhB concentration, and $Na_2S_2O_8$ concentration were investigated to find out the best conditions for efficient photocatalysis. By conducting a radical quenching test, all radicals of $HO^{\bullet}$, $SO_4^{\bullet-}$, $^1O_2$, and $O_2^{\bullet-}$ were found to be important in photocatalytic decomposition. The mechanism was proposed for the enhancement of photocatalytic RhB removal *via* band potential calculation, charge separation, surface redox reaction, and key reactive oxidation species. With its durability, reusability, and high efficiency, the Mn_2O_3/MIL-100(Fe) composite emerges as a potential photocatalyst working under visible light for application in wastewater treatment.

Introduction

The textile and dyeing industry is one of the main contributors to the economies of developing countries such as Vietnam. Dyes have become widely produced and used not only in the textile industry but also in the food industry and in biotechnology. Rhodamine B (RhB) is an organic dye that is representative of the group of xanthene dyes. It is widely used for coloring in the fiber industry, laboratory staining, and cytological testing because of its stable properties, fast coloring, and low cost as compared to other industrial color products. Therefore, the amount of wastewater from the textile industry in general, and RhB in particular, discharging into the water environment is very large, which brings many risks to ecosystems and human health.[1,2] Wastewater containing dyes is difficult to treat due to the persistent and complex structure of the dyes, which resist conventional biological treatment such as aerobic and anaerobic processes. As alternatives to biological treatment, physicochemical processes for the treatment of RhB have been studied extensively, including adsorption,[3,4] photocatalysis,[5–10] electrochemical-Fenton,[11] biological treatment, and filtration.[12] Among them, advanced oxidation processes, particularly photocatalysis, are usually considered as some of the most suitable techniques for the treatment of RhB and other dyes due to their being highly efficient, low-cost, and environment-friendly techniques. Persulfate-based photocatalysis has attracted much research attention since sulfate radical ($SO_4^{\bullet-}$) has advantages over hydroxyl radical in the degradation of organics in water such as faster reaction rate (10^6–10^9 M^{-1} s^{-1}), higher oxidation potential (2.5–3.1 V), longer lifetime (30–40 μs as compared to 1 μs of $HO^{\bullet}$), broader pH range, wider application, and higher degradation efficiency.[13,14] Sulfate radical can be generated by activation of persulfate *via* traditional methods such as using UV, heat, ultrasonication, transition metals, and photocatalysts.[15,16] Among them, the activation of persulfate by photocatalysis is usually considered as a green and promising route due to its low energy consumption, high recyclability, and lower photoexcited electron–hole recombination.

In recent years, manganese oxides have attracted more attention due to their practical application in many fields of study such as photocatalysis, fluorescence, gas sensors, electrochemical films, and lithium batteries. Among the manganese oxides, Mn_2O_3 is the most widely used photocatalyst under visible light, which exists in different morphologies[17–19] and can be prepared by different methods such as hydrothermal and precipitation.[19–21] Mn_2O_3 nanomaterials were synthesized and applied as photocatalysts for environment treatment such as degradation of ciprofloxacin,[21,22] decompositions of ammonium

[a]Faculty of Physical and Chemical Engineering, Le Quy Don Technical University, 236 Hoang Quoc Viet St., Bac Tu Liem District, Hanoi, Vietnam. E-mail: nguyentrungdung1980@gmail.com

[b]Faculty of Environment and Natural Resources, Ho Chi Minh City University of Technology (HCMUT), 268 Ly Thuong Kiet Street, District 10, Ho Chi Minh City, Vietnam. E-mail: nnhuy@hcmut.edu.vn

[c]Vietnam National University Ho Chi Minh City, Linh Trung Ward, Thu Duc City, Ho Chi Minh City, Vietnam

† Electronic supplementary information (ESI) available. See DOI: 10.1039/d1ra03496k

© 2021 The Author(s). Published by the Royal Society of Chemistry

Open Access Article. Published on 24 August 2021. Downloaded on 1/2/2026 2:42:14 AM. This article is licensed under a Creative Commons Attribution-NonCommercial 3.0 Unported Licence.

and nitrate to N_2,[23] reduction of CO_2,[24] and elimination of heavy metals such as As(III) and As(VI).[25] MIL-100(Fe), a type of metal–organic framework, has received lots of attention due to its hollow cage structure with a large specific surface area and high pore volume. Among preparation methods, the hydrothermal method is the preferred choice because of its simplicity, ease of implementation, and high efficiency.[26–31] In the environmental field, MIL-100(Fe) is also capable of removing many pollutants, such as heavy metals (Cr^{6+}),[29,31] RhB,[32,33] tetracycline antibiotic,[31] and microcystin-LR.[34] Although both Mn_2O_3 and MIL-100(Fe) can be used as photocatalysts under visible light due to their low bandgaps (*i.e.*, 1.44 eV and 2.6–2.7 eV, respectively), the high recombination of photoexcited electrons and holes in these two individual materials hinders their practical application for photocatalysis. Therefore, a composite of Mn_2O_3 and MIL-100(Fe) could be a potential material for enhancing photocatalytic activity *via* effective charge separation, which has not been reported in the literature.

In this study, Mn_2O_3/MIL-100(Fe) was synthesized by the hydrothermal method and applied for photocatalytic degradation of RhB under visible light irradiation and persulfate activation. Factors that affect the RhB degradation efficiency such as solution pH, material dosage, RhB concentration, and $Na_2S_2O_8$ concentration were investigated. Besides, durability and reusability tests were also conducted for evaluating the applicability of the material.

Experimental

Material synthesis and characterization

RhB was imported directly from Macklin (China). The chemicals for material synthesis (*e.g.*, $KMnO_4$, polyvinylpyrrolidone (PVP), iron powder, benzene-1,3,5-tricarboxylic acid (H_3BTC), and ethanol) and for photocatalytic experiments (*e.g.*, sodium persulfate, NaCl, NaOH, HNO_3, HCl, HF, and H_2SO_4) were all pure chemicals (≥99%) from China.

Mn_2O_3 was prepared by the hydrothermal method using $KMnO_4$ precursor.[21] At first, PVP solution was prepared by dissolving 1 g of PVP in 10 mL of ethanol and $KMnO_4$ solution was prepared by stirring 0.4789 g of $KMnO_4$ in 15 mL of double-distilled water. The two solutions were then mixed and vigorously stirred at room temperature for 10 min and transferred to a 100 mL Teflon autoclave containing 40 mL of hot double-distilled water at 90 °C. After that, the mixture was hydrothermally treated in the Teflon autoclave at 180 °C for 3 h and then allowed to cool to room temperature. The collected brown powder was centrifuged and rinsed several times with each of double-distilled water and ethanol. Finally, the material was subsequently dried at 80 °C for 12 h and heated at 700 °C for 4 h at a heating rate of 2 °C min^{-1} to obtain Mn_2O_3 black powder.

Mn_2O_3/MIL-100(Fe) materials with different weight ratios of MIL-100(Fe) (*i.e.*, 50, 60, 70, 80, and 90%) were synthesized by the hydrothermal method.[31] A pre-calculated amount of Mn_2O_3 was dispersed in a glass beaker containing 10 mL of double-distilled water and ultrasonically treated for 30 min. The suspension then had added to it 0.082 g of iron powder and 0.206 g of H_3BTC and stirred for 30 min. The suspension was subsequently transferred to the Teflon autoclave and hydrothermally treated at 150 °C for 4 days. After cooling down to room temperature, the material was centrifuged and rinsed with double-distilled water at 80 °C and ethanol at 60 °C before drying at 150 °C for 24 h. MIL-100(Fe) material was synthesized using the same procedure but without the addition of Mn_2O_3. The Mn_2O_3/MIL-100(Fe) composite was denoted as M100Mn. For comparison purposes, a physically mixed Mn_2O_3/MIL-100(Fe) material with a MIL-100(Fe)/Mn_2O_3 weight ratio of 60 : 40 was prepared by directly mixing pre-determined amounts of Mn_2O_3 and MIL-100(Fe) in ethanol under ultrasonication and stirring at room temperature for 48 h, following by centrifugation and drying at 80 °C for 12 h.

The synthesized materials were characterized by X-ray diffraction (XRD, D8 Advance, Bruker, Germany) for studying the crystalline structure and Fourier-transform infrared (FTIR) spectroscopy (Spectrum Two, PerkinElmer, USA) for exploring the surface bonding and functional groups. The morphology and the surface elemental composition of the materials were examined by scanning electron microscopy (SEM, S-4800, Hitachi, Japan) coupled with energy dispersive X-ray spectroscopy (EDX) and EMSA/MAS spectral data file. The surface area and porous structure of the materials were analyzed by the Brunauer–Emmett–Teller (BET) method using a surface area and porosity analyzer (TriStar II Plus 2.03, Micromeritics, USA). The UV-visible absorption spectra and the bandgap energy of the material were obtained by UV-visible diffuse reflectance spectroscopy using a spectrophotometer (V670, Jasco, Japan).

The pH_{pzc} of the material was determined by the titration method. Six conical flasks containing 12.5 mL of 0.1 M NaCl were prepared and the initial pH of these solutions (pH_i) was adjusted in the range of 2–11 by adding 0.1 M HCl or NaOH solutions. Each flask then had added to it 0.025 mg of material and was shaken for 48 h. After that, the material was removed by settling and filtering and the pH of the filtered solution was measured (pH_f). The pH_{pzc} was estimated at the pH_i value that does not change with the addition of the material ($pH_i = pH_f$).

Photocatalytic degradation of RhB

The photocatalytic activity of the material was evaluated through its ability for persulfate activation and photocatalytic degradation of RhB at room temperature (25 ± 2 °C) using a batch reactor. The light source in this experiment was a 40 W L4X LED, with the highest intensity at a wavelength of 446 nm. The distance from the lamp to the solution in a water-jacketed beaker was kept constant at 9 cm in all experiments. The pH of the RhB solution was adjusted by adding 0.05 M NaOH or H_2SO_4 solutions. Before photocatalytic tests, the photocatalyst was added into the RhB solution and stirred in the dark for 30 min to reach the adsorption equilibrium. After that, $Na_2S_2O_8$ was added to the solution and continuously aerated with air. The light was then turned on for photocatalytic reaction. During the experiment, 4 mL of the sample was taken, centrifuged, and sent for RhB analysis by measuring the absorbance at 554 nm using a spectrophotometer (Libra SP60, Biochrom, UK).

To determine the suitable conditions for photocatalytic degradation of RhB using M100Mn, the affecting factors were

Open Access Article. Published on 24 August 2021. Downloaded on 1/2/2026 2:42:14 AM.
This article is licensed under a Creative Commons Attribution-NonCommercial 3.0 Unported Licence.

investigated in a range of solution pH (2–11), photocatalyst dosage (0–1000 mg L^{-1}), RhB concentration (15–50 mg L^{-1}), and $Na_2S_2O_8$ concentration (100–500 mg L^{-1}). To evaluate the reusability of the material, the photocatalyst was separated from the dye solution by centrifugation after each reaction cycle and then washed with water and ethanol to remove the RhB on the surface of the catalyst. Next, the material was dried in a vacuum oven at 80 °C for 5 h before using it for the next cycle. Each cycle of the photocatalytic reaction was performed in the presence of $Na_2S_2O_8$ and under aeration conditions. To determine the major reactive oxygen species, a quenching test was conducted by adding radical scavenging agents with a concentration of 10 mM, namely ethylenediaminetetraacetic acid disodium salt (EDTA-2Na, for photoexcited holes h^+), *tert*-butanol (TBA, for $HO^\bullet$), *p*-benzoquinone (*p*-BQ, for $O_2^{\bullet-}$), furfuryl alcohol (FFA, for $^1O_2$ and $HO^\bullet$), and phenol (PheOH, for $SO_4^{\bullet-}$ and $HO^\bullet$), before turning on the light for the photocatalytic reaction.

All the photocatalytic experiments were repeated 3 times and the average values were reported in this study. The RhB degradation efficiency (H, %) and the rate constant of the pseudo-first-order kinetic model (k_{app}, min^{-1}) were determined by the following formulas:

$$H\ (\%) = \frac{C_0 - C_t}{C_0} \times 100 \quad (1)$$

$$\ln\left(\frac{C_t}{C_0}\right) = -k_{app} \times t \quad (2)$$

where C_0 and C_t (mg L^{-1}) are the concentrations of RhB at the initial and determined times, respectively.

Results and discussion

Characteristics of the synthesized materials

XRD patterns of Mn_2O_3, MIL-100(Fe), and M100Mn(60 : 40) materials are plotted in Fig. 1(a). In the XRD pattern of Mn_2O_3, diffraction peaks are observed at 2θ of 23.2, 33.0, 38.3, 45.2, 49.4, 55.2, and 65.9°, corresponding to the planes of (211), (222), (400), (332), (431), (440), and (622) of Mn_2O_3 crystals (JCPDS card no. 41-1442). Diffraction peaks of MIL-100(Fe) are located at 2θ of 3.4, 4.0, 5.9, 6.8, 7.0, 10.2, 10.8, and 11.0°, assigned to the planes (220), (311), (511), (660), (842), (440), (600), and (422).[29,35,36] In addition, no other impurity peaks were detected, which demonstrates that the synthesized MIL-100(Fe) and Mn_2O_3 are of high purity and well crystallized. The XRD peaks of the M100Mn(60 : 40) material are in good agreement with the respective peaks of Mn_2O_3 and MIL-100(Fe), demonstrating the successful synthesis of Mn_2O_3/MIL-100(Fe) with a good combination between the two materials.

As seen in Fig. 1(b), there are two bands at 645.9 and 558.34 cm^{-1} in the FTIR spectrum of Mn_2O_3, which are assigned to the characteristic Mn–O stretching vibration of Mn(III) oxide.[37,38] In the MIL-100(Fe) spectrum, a peak at 3380.21 cm^{-1} is attributed to the vibration of the O–H group, showing the presence of adsorbed water. The strong peaks at 812 and 710.89 cm^{-1} are characteristic of the 1,3,5-tri-substitution of the benzene ring. The peaks observed at 1628.86, 1450.31, and 1382.54 cm^{-1} are assigned to asymmetrical and symmetrical vibrations of the corresponding carboxyl group. The high-intensity peak at 1709 cm^{-1} corresponds to the stretching vibration of the C=O group in 1,3,5-BTC. There is also a peak at 459.01 cm^{-1} associated with Fe–O stretching vibrations. The above results showed that the MIL-100(Fe) structure contains the 1,3,5-BTC base frame while losing the bond of the carboxyl group of 1,3,5-BTC, proving the bond formation of Fe ions and organic ligand of 1,3,5-H_3BTC, which is consistent with previous studies.[28,31] The decrease of Mn_2O_3 peak intensity and the presence of MIL-100(Fe) peak in the spectrum of the M100Mn(60 : 40) material proved the successful synthesis of Mn_2O_3/MIL-100(Fe) composite by the hydrothermal method (Fig. 1(b)).

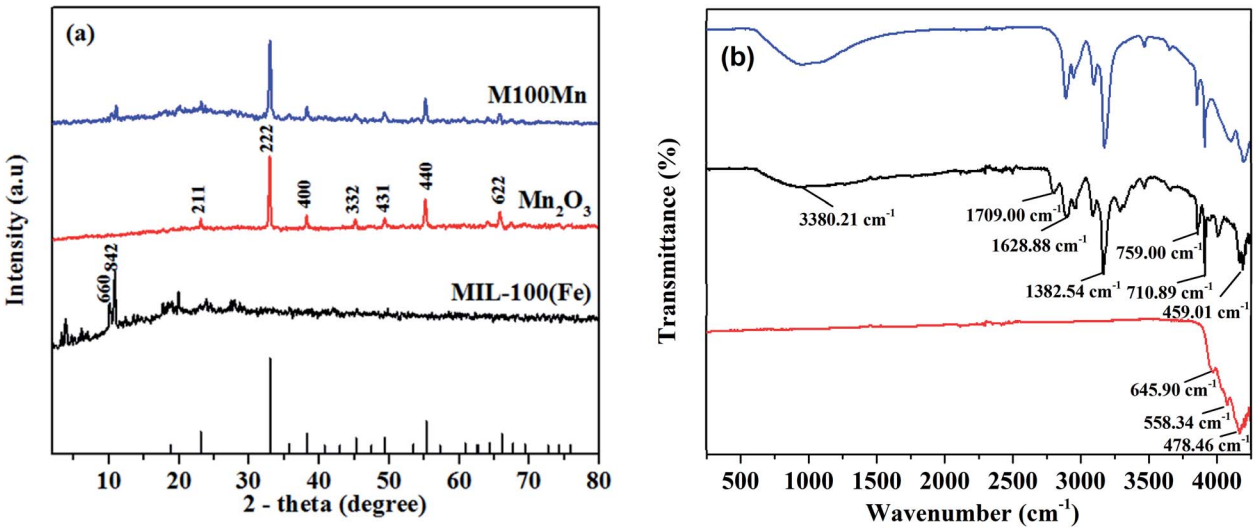

Fig. 1 (a) XRD patterns and (b) FTIR spectra of Mn_2O_3, MIL-100(Fe), and M100Mn(60 : 40).

 © 2021 The Author(s). Published by the Royal Society of Chemistry

Open Access Article. Published on 24 August 2021. Downloaded on 1/2/2026 2:42:14 AM.
This article is licensed under a Creative Commons Attribution-NonCommercial 3.0 Unported Licence.

Fig. 2 shows the SEM results of the synthesized materials. As seen in Fig. 2(a), Mn_2O_3 has a relatively uniform particle size in the range of 100–150 nm, which is consistent with previous publications.[38] Regarding MIL-100(Fe) (Fig. 2(b)), it has irregular polyhedral morphologies with particle size from 150 to 600 nm, which is also consistent with previous results from the literature.[34,39] The morphology of M100Mn(60 : 40) is similar to that of Mn_2O_3, but with a rougher surface (Fig. 2(c)), resulting from the combined structure of Mn_2O_3 and MIL-100(Fe). EDX result reveals that the main components of the M100Mn(60 : 40) material are Fe, Mn, C, and O (Fig. S1 of ESI†), proving that the M100Mn material was successfully synthesized with a combination of MIL-100(Fe) and Mn_2O_3 without other impurities.

The N_2 adsorption–desorption isotherms, as well as the pore size distributions, of Mn_2O_3, MIL-100(Fe), and M100Mn(60 : 40) materials are presented in Fig. 3(a) and S2.† Mn_2O_3 shows a slightly porous structure and its isotherm can be classified as a type III adsorption isotherm. It has a low surface area of 12.51 $m^2\ g^{-1}$, a low pore volume of 0.051 $cm^3\ g^{-1}$, and a large pore size of 20.28 nm. In contrast, MIL-100(Fe) shows a highly porous structure with a type II adsorption isotherm, a very high surface area of 1160.73 $m^2\ g^{-1}$, a high pore volume of 0.67 $cm^3\ g^{-1}$, and a very low pore size of 1.94 nm. Hence, the porous structure of Mn_2O_3 was significantly increased when combined with highly porous MIL-100(Fe) material, making M100Mn(60 : 40) exhibit a type II adsorption isotherm with a high surface area of 766.45 $m^2\ g^{-1}$, a pore volume of 0.30 $cm^3\ g^{-1}$, and a pore size of 3.22 nm. Therefore, the structure of M100Mn(60 : 40) is not only highly crystalline (from XRD results) but also highly porous with uniform pore size distribution (from BET results), which could be promising for adsorption and photocatalytic applications.

The results from UV-visible light absorption of the materials are presented in Fig. 3(b). The bandgap energies of Mn_2O_3, MIL-100(Fe), and M100Mn were calculated *via* the Kubelka–Munk equation to be 1.44, 2.94, and 2.72 eV, respectively, which are consistent with previous results in the literature.[21–23,29,32,40] From the UV-visible absorption spectra, the absorption edges of the Mn_2O_3, MIL-100(Fe), and M100Mn(60 : 40) materials were determined to be 861, 420, and 454 nm, respectively. The visible light absorption of M100Mn was improved as compared to MIL-100(Fe) due to the combination with Mn_2O_3. This proved the successful combination of Mn_2O_3 and MIL-100(Fe) in the composite structure of the M100Mn material. The enhancement of visible light absorption can improve the light-harvesting ability, suggesting an improvement of the photocatalytic activity of the M100Mn material under visible light conditions.

The thermal stability of Mn_2O_3, MIL-100(Fe), and M100Mn(60 : 40) was examined by TGA from 50 to 900 °C, and the results are shown in Fig. 4. When the temperature increases, the weight of the Mn_2O_3 material is almost unchanged, indicating that the Mn_2O_3 material is stable in the temperature range up to 900 °C. When the temperature is raised above 900 °C, Mn_2O_3 would be converted to Mn_3O_4.[41,42] Regarding MIL-100(Fe), there are 3 stages of weight loss observed. The first stage of 31.9% weight loss in the temperature range of 50–150 °C corresponds to the removal of physically adsorbed water molecules trapped inside the pore of MIL-100(Fe). The second stage with a very low weight loss of 3.20% at 150–350 °C is attributed to the removal of chemically adsorbed water molecules and carboxylic groups, proving that MIL-100(Fe) is stable in this temperature range. Significant weight loss of 74.403% is observed in the third stage with a temperature range of 350–410 °C. At above 350 °C, the structural collapse of MIL-100(Fe) upon ligand decomposition involves H_3BTC combustion, MOF structure destruction, and organic matter evaporation. A significant weight loss then begins at 400 °C, due to the continuing breakdown of the framework accompanied by a reduction in the amount of iron present in the structure. The degradation of the third stage ends at 410 °C, indicating that MIL-100(Fe) is completely decomposed to Fe_2O_3. Hence, the overall thermal stability of the synthesized MIL-100(Fe) sample is determined at below 350 °C, which should be activated at a temperature between 150 and 350 °C before application for adsorption and catalysis.[43–46]

The overall trend of weight loss in the M100Mn(60 : 40) material is similar to that in MIL-100(Fe). The weight loss is attributed to the loss of water molecules and solvents below 250 °C. Framework breakdown of both MIL-100(Fe) and M100Mn(60 : 40) composite material occurs in the range 250–381 °C due to the carboxyl breakdown of trimesic acid. Therefore, the new composite material is stable below 250 °C. The structure collapses after being heated at temperatures greater than 381 °C, indicating that M100Mn(60 : 40) is more thermally stable than MIL-100(Fe) because of its thermal stability enhancement from combination with Mn_2O_3 and that the effect

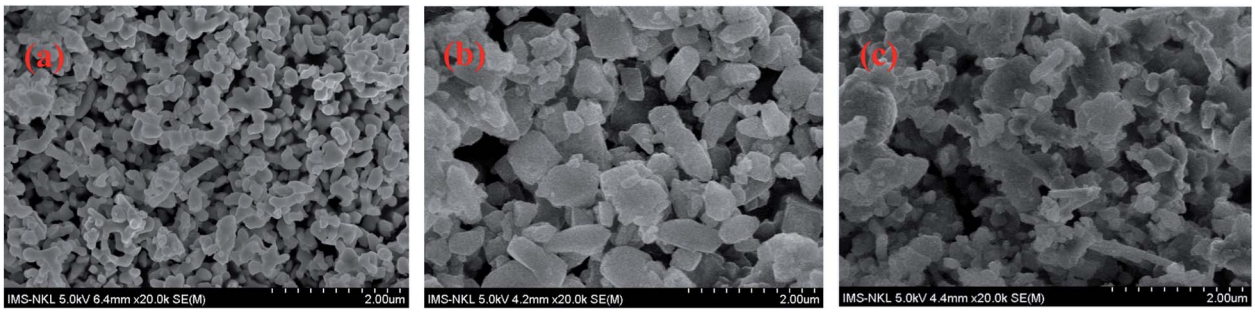

Fig. 2 SEM images of (a) Mn_2O_3, (b) MIL-100(Fe), and (c) M100Mn(60 : 40).

Open Access Article. Published on 24 August 2021. Downloaded on 1/2/2026 2:42:14 AM.
This article is licensed under a Creative Commons Attribution-NonCommercial 3.0 Unported Licence.

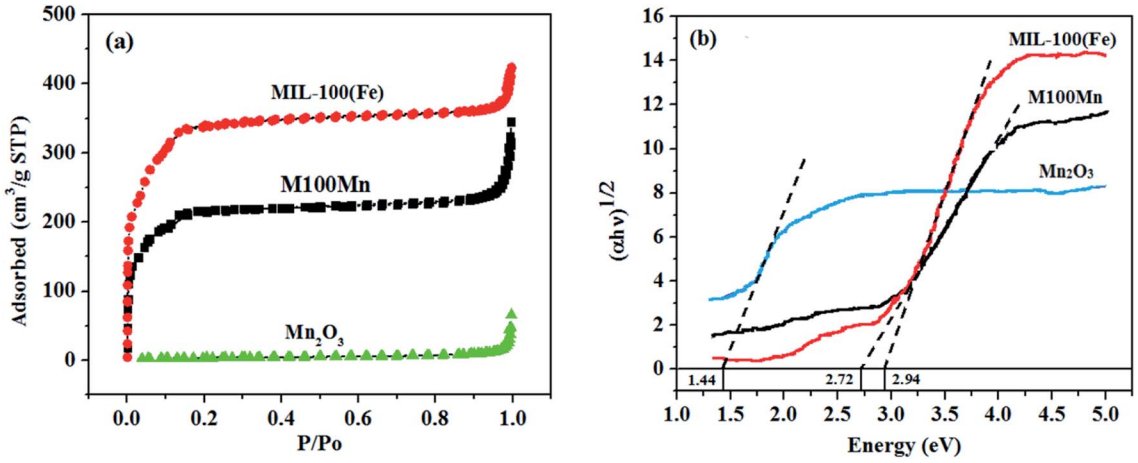

Fig. 3 (a) The N_2 adsorption–desorption isotherms and (b) plots of $(\alpha h\nu)^{1/2}$ *versus* $h\nu$ for Mn_2O_3, MIL-100(Fe), and M100Mn(60 : 40) photocatalysts.

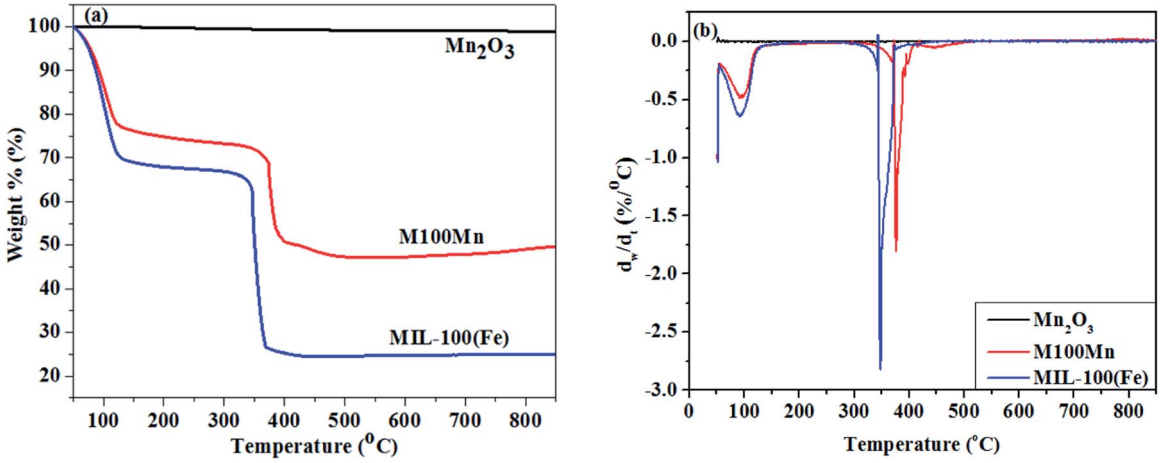

Fig. 4 (a) TGA curves and (b) DTG curves of Mn_2O_3, MIL-100(Fe), and M100Mn (60 : 40) materials.

of temperature on the stability of the material can be ignored during the photocatalytic process.

Photocatalytic degradation of RhB using the M100Mn(60 : 40) material

The pH value is of significance and has an impact on the adsorption capacity and reaction rate of heterogeneous catalytic reactions, thus affecting the entire photocatalytic process as well as the efficiency of the reaction. Fig. 5(a) presents the effect of pH on the photocatalytic degradation of RhB using the M100Mn/$Na_2S_2O_8$/RhB/Vis system with RhB concentration of 25 mg L^{-1}, M100Mn dosage of 500 mg L^{-1}, $Na_2S_2O_8$ concentration of 300 mg L^{-1}, and temperature of 25 °C. The RhB degradation efficiency after 90 min of reaction increased from 93.92% at pH 2 to 95.91% at pH 3, but then gradually decreased to 76.42% with a further increase of pH up to 11. The better performance of the M100Mn material can be explained by its isoelectric point, which was determined as pH_{pzc} of 4.65 (Fig. S3†). When the solution pH is less than pH_{pzc}, the surface of the material is positively charged and promotes the adsorption of persulfate anion ($S_2O_8^{2-}$) onto the surface, and thereby enhancing persulfate activation ability to form reactive oxygen species. When the solution pH is greater than pH_{pzc}, the negative surface of the material reduces the persulfate anion adsorption and thus reduces the treatment efficiency. However, at pH 2, the amount of proton H^+ exceeds a certain threshold, which leads to a decrease in the reaction rate. Therefore, the acidic condition is favorable for photocatalytic reaction and pH 3 (with RhB degradation rate constant of 0.0393 min^{-1}; Fig. S4†) was then chosen for further investigations.

The degradation of RhB was studied under different conditions of visible light, $Na_2S_2O_8$, and catalyst presence, and the results are presented in Fig. 5(b). Photolysis alone (*i.e.*, Vis: visible light only, without $Na_2S_2O_8$ and photocatalyst) led to very low RhB degradation, which can be negligible during the reaction. Adding $Na_2S_2O_8$ under visible light irradiation (*i.e.*, $Na_2S_2O_8$/Vis) enhanced the RhB degradation efficiency to 28.69%. Although it is a notable improvement, this photolytic

 © 2021 The Author(s). Published by the Royal Society of Chemistry

Open Access Article. Published on 24 August 2021. Downloaded on 1/2/2026 2:42:14 AM.
This article is licensed under a Creative Commons Attribution-NonCommercial 3.0 Unported Licence.

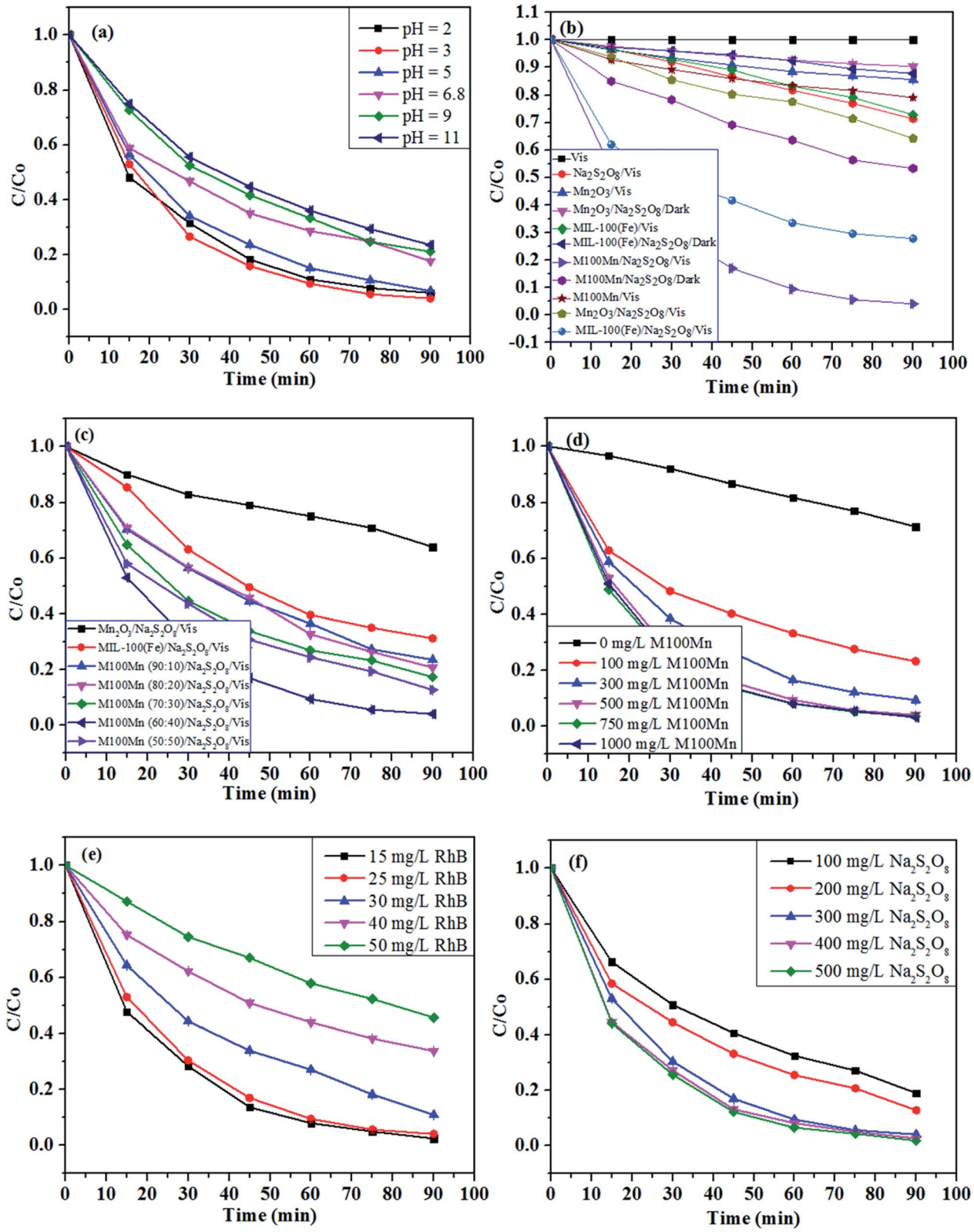

Fig. 5 Effects of (a) solution pH, (b) reaction systems, (c) MIL-100(Fe) : Mn_2O_3 weight ratio, (d) M100Mn dosage, (e) RhB concentration, and (f) $Na_2S_2O_8$ concentration on the photocatalytic degradation efficiency of RhB.

oxidation cannot be used due to its still low degradation efficiency. Without $Na_2S_2O_8$, the RhB photocatalytic degradation efficiencies after 90 min using Mn_2O_3, MIL-100(Fe), and M100Mn were 14.38, 27.21, and 21.59%, respectively, under visible light. In the presence of $Na_2S_2O_8$ but without visible light, the chemical degradation efficiencies using these

Open Access Article. Published on 24 August 2021. Downloaded on 1/2/2026 2:42:14 AM.
This article is licensed under a Creative Commons Attribution-NonCommercial 3.0 Unported Licence.

materials were 9.71, 12.23, and 46.74%, respectively. The photocatalytic RhB degradation efficiencies under visible light and persulfate activation of pure Mn_2O_3 and MIL-100(Fe) were low at 35.97 and 68.77%, respectively, which is due to the rapid recombination of photoexcited electron and hole pairs in these two materials. Meanwhile, the RhB degradation efficiency was greatly enhanced to 95.91% when using the M100Mn composite. The RhB degradation rate constant using M100Mn was 7.72 and 2.67 times higher than when using Mn_2O_3 and MIL-100(Fe), respectively (Fig. S5†). This proves the enhancement of electron transfer between single materials in the composite, thus reducing the electron–hole recombination potential and improving the photocatalytic activity. Meanwhile, the presence of $Na_2S_2O_8$ would increase the formation of reactive oxygen species, thus significantly improving the photocatalytic efficiency of the material, proving the important role of the simultaneous presence of photocatalyst, visible light, and $Na_2S_2O_8$ in RhB degradation.

The effect of MIL-100(Fe) content (*i.e.*, 50–90%) on the photocatalytic performance of M100Mn is illustrated in Fig. 5(c). The degradation efficiency increased from 87.26 to 95.91% with an increase of MIL-100(Fe) content from 50 to 60% but gradually decreased to 76.49% with a further increase of MIL-100(Fe) content up to 90%. The M100Mn composite with the MIL-100(Fe) : Mn_2O_3 weight ratio of 60 : 40 had the highest RhB degradation efficiency with a rate constant of 2.28, 2.11, 1.95, and 1.70 higher than those of M100Mn material with MIL-100(Fe) : Mn_2O_3 weight ratio of 90 : 10, 80 : 20, 70 : 30, and 50 : 50, respectively (Fig. S6†).

The photocatalytic activities of M100Mn(60 : 40) composites synthesized by the hydrothermal and physical mixing methods were also compared. As seen in Fig. S7,† the RhB degradation efficiency after 90 min of reaction was 95.91% for M100Mn(60 : 40) prepared by the hydrothermal method and 80.53% for that prepared by the physical mixing method. The RhB degradation rate constant of M100Mn(60 : 40) prepared by the hydrothermal method was 1.9 times higher than that of M100Mn(60 : 40) prepared by the mixing method. The physical mixing method has the advantages of simplicity and ease of operation. However, it is hard to achieve the highly homogeneous dispersion of small Mn_2O_3 on the surface of the MIL-100(Fe) material. Moreover, the physical links between the two materials in the physical mixing method are not as good as those in the hydrothermal method. These issues could result in high electron–hole recombination in each material, which decreases the photocatalytic activity.[47,48]

The UV-visible absorption spectrum of RhB in Fig. S8† shows that the characteristic absorption peak at 554 nm of RhB did not shift during the reaction period. The spectral intensity decreased sharply after the first 15 min and almost disappeared after 90 min. The M100Mn composite is effective for the activation of $Na_2S_2O_8$ to form reactive oxygen species, which can completely break down the structure of RhB.[49]

The effect of M100Mn(60 : 40) dosage (in the range of 0–1000 mg L^{-1}) on RhB degradation efficiency is demonstrated in Fig. 5(d). At low dosages, the degradation of RhB increased from 28.69 to 95.91% with an increase of the catalyst dosage from 0 to 500 mg L^{-1} (Fig. 5(d)), corresponding to an increase of rate constant from 0.0038 to 0.0363 min^{-1} (Fig. S9†). However, when the catalyst dosage increased from 500 to 1000 mg L^{-1}, the RhB degradation changed insignificantly. It can be explained in that an increase in the catalyst dosage results in an increase in surface active sites for photocatalysis as well as persulfate activation and thus reactive oxygen species formation for faster RhB degradation.[8,50] However, when the content of M100Mn catalyst material is in excess, there is not sufficient persulfate activation at a constant $Na_2S_2O_8$ concentration, resulting in the unchanged degradation efficiency. Therefore, 500 mg L^{-1} was chosen as a suitable M100Mn dosage for further experiments.

Fig. 5(e) presents the degradation efficiency of RhB under different initial RhB concentrations from 15 to 50 mg L^{-1}. It can be seen that the degradation efficiency decreased continuously with an increase of RhB concentration. As provided in Fig. S10,† the rate constant gradually decreased from 0.0404 to 0.0086 min^{-1} when the RhB concentration increased from 15 to 50 mg L^{-1}. This can be explained by the fact that an increase in the number of dye molecules leads to a longer time to complete the RhB decomposition, resulting in a decrease in treatment efficiency.[51] Besides, the rate of the photocatalytic reaction depends largely on the formation of reactive oxygen species on the photocatalytic surface and on the types of reactive oxygen species that are produced to attack and weaken the structure of RhB.[51,52] The increase in the initial concentration of RhB causes a large amount of adsorbed RhB on the active centers of the catalyst, thus interfering with the adsorption of $S_2O_8^{2-}$ on the surface and reducing the rate of formation of reactive oxygen species (*e.g.*, sulfate and hydroxyl radicals) and therefore the degradation of RhB. Besides, an increase of RhB concentration could prevent the transmission of light in the solution, thus reducing the ability of the photocatalyst to absorb photons, resulting in a significant reduction in photocatalytic degradation. Therefore, an RhB concentration of 25 mg L^{-1} was then chosen for subsequent experiments.

The effect of the $Na_2S_2O_8$ concentration on the degradation of RhB is shown in Fig. 5(f). It is obvious that the degradation of RhB was proportional to the $Na_2S_2O_8$ concentration. When the concentration of $Na_2S_2O_8$ increased from 100 to 300 mg L^{-1}, the RhB degradation efficiency after 90 min increased from 81.01 and 95.91% (Fig. 5(f)), and the rate constant increased from 0.0172 to 0.0363 min^{-1} (Fig. S11†). This is because the increase in $Na_2S_2O_8$ concentration enhances the persulfate activation to produce more reactive oxygen species, which leads to a corresponding increase in RhB degradation. However, when using high $Na_2S_2O_8$ concentrations of 400 and 500 mg L^{-1}, both the degradation efficiency and rate constant did not change significantly. The reason may be due to the side effect of excessive $Na_2S_2O_8$ forming a weaker oxidizing radical ($S_2O_8^{\cdot-}$) as in Re. (3). Therefore, a $Na_2S_2O_8$ concentration of 300 mg L^{-1} was selected for the subsequent experiments.

$$S_2O_8^{2-} + SO_4^{\cdot-} \rightarrow SO_4^{2-} + S_2O_8^{\cdot-} \quad (3)$$

The reusability and stability of the catalyst are significant indicators of its feasibility and applicability in practice. The

 © 2021 The Author(s). Published by the Royal Society of Chemistry

Open Access Article. Published on 24 August 2021. Downloaded on 1/2/2026 2:42:14 AM.
This article is licensed under a Creative Commons Attribution-NonCommercial 3.0 Unported Licence.

reusability of the prepared M100Mn was evaluated *via* five cycles of reaction. As shown in Fig. 6(a), the RhB degradation efficiency slightly decreased from 95.91 to 91.78% after the first three cycles, and to 77.96% after the two next cycles, proving its relatively good recyclability and stability. The reduction in the RhB degradation efficiency can be attributed to the partial destruction of the photocatalyst structure and the loss of some photocatalyst mass during washing for reuse. Also, the adsorbed RhB or intermediates and by-products on the photocatalyst during the previous test were not completely eliminated, causing a decrease in the RhB degradation in the subsequent cycles.

Besides, the durability of M100Mn after five cycles was evaluated by FTIR (Fig. 6(b)). The FTIR characteristic peaks of the M100Mn material were not significantly changed after five cycles of reuse, showing that the material was not poisoned by intermediates of the process of RhB degradation. However, the intensity of the characteristic peak slightly decreased after the first three cycles and obviously decreased after the fourth and fifth cycles, signifying the loss of metal ions from the surface of the photocatalyst. This is evidenced by the significant decrease in the peak at a wavenumber of 459.01 cm^{-1} corresponding to the Fe–O bond after the fifth cycle.

Proposed mechanism for photocatalytic degradation of RhB by the M100Mn material

In a regular photocatalytic reaction, photoexcited holes (h^+), superoxide radical ($O_2^{\bullet-}$), and hydroxyl radical ($HO^\bullet$) are usually the main reactive species for the degradation of organic pollutants in water.[53] In this study, radical scavengers TBA, PheOH, FFA, *p*-BQ, and EDTA-2Na with a concentration of 10 mM were used for quenching the oxidation activity of $HO^\bullet$, $SO_4^{\bullet-}/HO^\bullet$, $^1O_2/HO^\bullet$, $O_2^{\bullet-}$, and h^+, respectively. There was a decrease in the RhB degradation rate constant (see Fig. S12†) and efficiency (see Fig. 7) from 95.91% (without scavengers) to

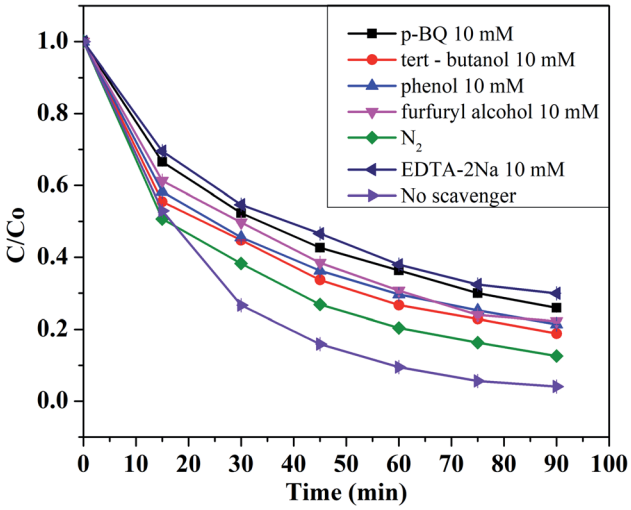

Fig. 7 Degradation efficiency of RhB in the presence of different radical scavengers.

81.14, 78.10, 77.77, 74.04, and 70.01% in the presence of TBA, PheOH, FFA, *p*-BQ, and EDTA-2Na, respectively. However, these insignificant reductions indicate that $HO^\bullet$, $SO_4^{\bullet-}$, $^1O_2$, $O_2^{\bullet-}$, and h^+ play important roles in the photocatalytic degradation of RhB under visible light and persulfate activation. Besides, a decrease in RhB degradation efficiency after 90 min of reaction from 95.91% (under air aeration) to 87.39% (with N_2 aeration) proved the important role of oxygen in the photocatalytic reaction, suggesting the contribution of O_2 as an electron scavenger for reducing the electron–hole recombination and as a source for the formation of $O_2^{\bullet-}$ radicals.

A comparison of M100Mn with other materials for persulfate activation for RhB removal is summarized in Table 1. Although the tested conditions were different for each study, the M100Mn/PS/Vis system at the optimum conditions in this study

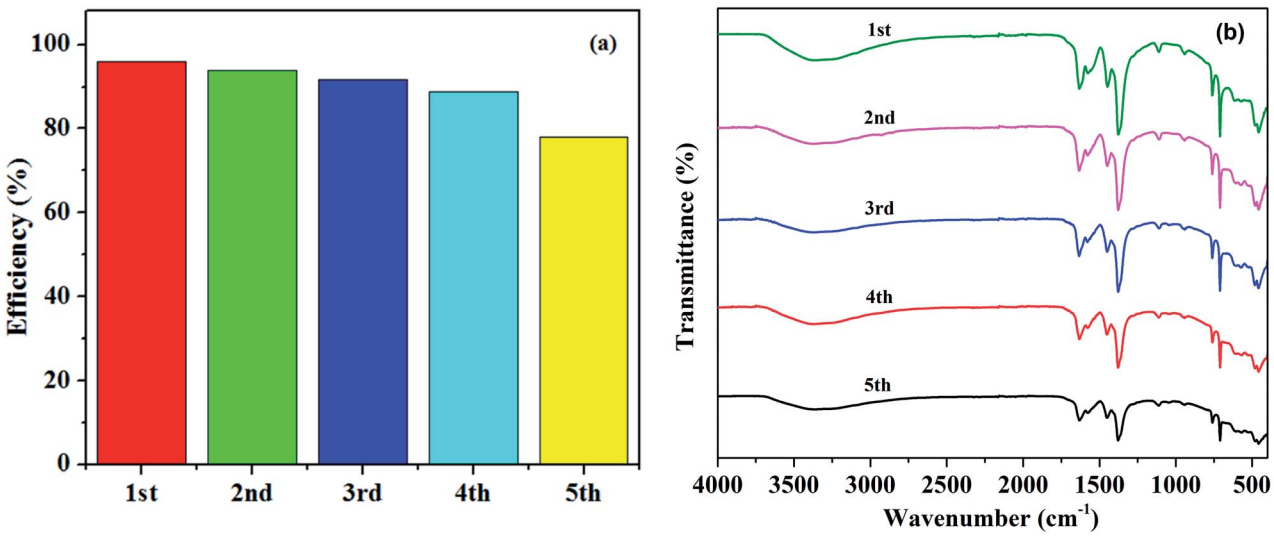

Fig. 6 (a) Degradation efficiency of RhB during five times of reusing the M100Mn material and (b) FTIR spectrum of M100Mn(60 : 40) after each of the five cycles.

Open Access Article. Published on 24 August 2021. Downloaded on 1/2/2026 2:42:14 AM.
This article is licensed under a Creative Commons Attribution-NonCommercial 3.0 Unported Licence.

shows many advantages such as using environment-friendly Fe and Mn, removal of high RhB concentration (25 mg L^{-1}) within a short time (90 min), low persulfate consumption (1.26 mM), and especially use of low-cost LED light, all of which are promising for large-scale application.

The mechanism for photocatalytic removal of RhB under visible light and persulfate activation relates to the charge transfer on the surface of the M100Mn material. The energy levels of valance band (E_{VB}) and conduction band (E_{CB}) are calculated *via* bandgap energy (E_g) by the following equations.[54,55]

$$E_{VB} = X - E_e + 0.5 \times E_g \quad (4)$$

$$E_{CB} = E_{VB} - E_g \quad (5)$$

where X is the electronegativity of the material and E_e is the energy of free electron ($\approx$4.5 eV *vs.* SHE).

From UV-visible diffuse reflectance spectroscopy results, the bandgap energies of MIL-100(Fe) and Mn_2O_3 materials were determined to be 2.94 eV and 1.44 eV, respectively. The E_{VB} and E_{CB} values were then calculated to be 2.44 and −0.5 eV, respectively, for MIL-100(Fe), and 0.34 and −1.1 eV, respectively, for Mn_2O_3. Based on these band energy values, the combination of Mn_2O_3 and MIL-100(Fe) in M100Mn material as well as its mechanism for removal of RhB is proposed in Fig. 8.

Under visible light irradiation, the electrons (e^-) from the valance bands of Mn_2O_3 and MIL-100(Fe) jump to the

Table 1 RhB removal by various heterogeneous catalysts with persulfate activation

Catalyst	Reaction conditions	Performance	Reference
Mn_2O_3/MIL-100(Fe) (60%)	RhB: 25 mg L^{-1}; catalyst: 500 mg L^{-1}; persulfate: 1.26 mM; pH 3.0; temperature: 25 °C; lamp: LED (40 W)	95.91% of RhB was removed in 90 min with k_{app} = 0.0363 min^{-1}; $HO^{\bullet}$, $SO_4^{\bullet-}$, $^1O_2$, $O_2^{\bullet-}$, and h^+ play important roles in the photocatalytic degradation of RhB	This work
MIL-88A	RhB: 10 mg L^{-1}; catalyst: 500 mg L^{-1}; persulfate: 1.68 mM; pH 3.0; temperature: 40 °C; lamp: UVA (9 W)	80% of RhB was removed in 120 min with k_{app} = 0.131 min^{-1}; $SO_4^{\bullet-}$ and $HO^{\bullet}$ were the main reactive oxygen species determining the RhB oxidation	60
MIL-53(Fe)/BiOCl (0.6 : 1)	RhB: 20 mg L^{-1}; catalyst: 500 mg L^{-1}; persulfate: 2.1 mM; pH 3.0; temperature: 25 °C; lamp: xenon (350 W) with a 420 nm cut-off filter	99.5% of RhB was removed in 30 min with k_{app} = 0.157 min^{-1}; $SO_4^{\bullet-}$ and $HO^{\bullet}$ were the main reactive oxygen species, along with electrons and holes (h^+), determining the RhB oxidation	61
Fe^0/C_3N_4	RhB: 20 mg L^{-1}; catalyst: 400 mg L^{-1}; persulfate: 3 mM; pH 3.5; temperature: 30 °C; lamp: metal halide–xenon (350 W) with a 400 nm cut-off filter	97% of RhB was removed in 40 min with k_{app} = 0.156 min^{-1}; h^+ and $SO_4^{\bullet-}$ played important roles in the oxidation process	8
CeO_2@LDH	RhB: 10 mg L^{-1}; catalyst: 400 mg L^{-1} persulfate: 6 mM; pH 7.0; temperature: 30 °C; lamp: xenon (50 W) with a 400 nm cut-off filter	96.9% of RhB was removed in 30 min with k_{app} = 0.0809 min^{-1}; $SO_4^{\bullet-}$, $O_2^{\bullet-}$, and $HO^{\bullet}$ were the main reactive oxygen species determining the RhB oxidation	62
BiOI/Fe_3O_4 (5 : 1)	RhB: 20 mg L^{-1}; catalyst: 500 mg L^{-1} persulfate: 1 mM; pH 4.6; temperature: 25 °C; lamp: xenon (500 W) with a 420 nm cut-off filter	98.4% of RhB was removed in 30 min with k_{app} = 0.130 min^{-1}; $SO_4^{\bullet-}$ and $HO^{\bullet}$ were the main reactive oxygen species, along with photoexcited holes (h^+), determining the RhB oxidation	58
TiO_2/FeOCl (20%)	RhB: 5 mg L^{-1}; catalyst: 400 mg L^{-1}; persulfate: 1.48 mM; no pH adjustment; temperature: 25 °C; lamp: LED (50 W)	64.6% of RhB was removed in 90 min with k_{app} = 0.0378 min^{-1}; $SO_4^{\bullet-}$, $O_2^{\bullet-}$, and $HO^{\bullet}$ were the main reactive oxygen species, along with photoexcited holes (h^+), determining the RhB oxidation	63
TiO_2/carbon dots	RhB: 5 mg L^{-1}; catalyst: 400 mg L^{-1}; persulfate: 1.48 mM; no pH adjustment; temperature: 25 °C; lamp: LED (50 W)	67% of RhB was removed in 240 min with k_{app} = 0.0439 min^{-1}; $SO_4^{\bullet-}$ and $O_2^{\bullet-}$ were the main reactive oxygen species, along with photoexcited holes (h^+), determining the RhB oxidation	64
ZnO/$CuBi_2O_4$ (5%)	RhB: 5 mg L^{-1}; catalyst: 400 mg L^{-1}; persulfate: 1.48 mM; no pH adjustment; temperature: 25 °C; lamp: LED (50 W)	100% of RhB was removed in 210 min with k_{app} = 0.0178 min^{-1}; $SO_4^{\bullet-}$, $O_2^{\bullet-}$, and $HO^{\bullet}$ were the main reactive oxygen species, along with photoexcited holes (h^+), determining the RhB oxidation	65
ZnS/$ZnFe_2O_4$	RhB: 20 mg L^{-1}; catalyst: 400 mg L^{-1}; persulfate: 0.37 mM; no pH adjustment; temperature: 25 °C; lamp: low-pressure mercury UV (6 W, 254 nm)	97.67% of RhB was removed in 90 min with k_{app} = 0.03815 min^{-1}; $SO_4^{\bullet-}$, $O_2^{\bullet-}$, and $HO^{\bullet}$ were the main reactive oxygen species determining the RhB oxidation	66

 © 2021 The Author(s). Published by the Royal Society of Chemistry

Open Access Article. Published on 24 August 2021. Downloaded on 1/2/2026 2:42:14 AM.
This article is licensed under a Creative Commons Attribution-NonCommercial 3.0 Unported Licence.

corresponding conduction bands of the materials and leave holes (h^+) in the valance bands (Re. (6)). These photoexcited electron–hole pairs are easily recombined together with a very short lifetime unless they are separated and consumed. In the M100Mn material, the electromagnetic field at the interface of Mn_2O_3 and MIL-100(Fe) helps to move the electrons and holes in opposite ways.[56] Specifically, the electrons from the conduction band of Mn_2O_3 transfer to the conduction band of MIL-100(Fe) with higher potential. In contrast, the holes from the valence band of MIL-100(Fe) transfer to the valance band of Mn_2O_3 with lower potential. Hence, the recombination of electrons and holes is effectively limited and they can easily move to the surface of the corresponding materials for participating in the reduction and oxidation reactions. Since the E_{CB} of MIL-100(Fe) is more negative than the potential of the $O_2/O_2^{\bullet-}$ redox couple (−0.33 V), the electrons are oxidized by dissolved oxygen (O_2) and persulfate ($S_2O_8^{2-}$) to form superoxide radicals ($O_2^{\bullet-}$) (Re. (7)) and sulfate radicals ($SO_4^{\bullet-}$) (Re. (8)). This process fosters the electron transfer from Mn_2O_3 to MIL-100(Fe) and inhibits photoexcited electron–hole recombination. On the other hand, the E_{VB} of Mn_2O_3 is lower than the potential of the $H_2O/HO^\bullet$ redox couple (2.4 V); thus the photoexcited holes on Mn_2O_3 cannot react with H_2O to produce hydroxyl radical ($HO^\bullet$), which is consistent with the above described h^+ quenching test by using EDTA-2Na. Here, h^+ directly oxidize RhB into products and intermediates. Besides, the sulfate radicals in the solution could react with water to produce hydroxyl radical ($HO^\bullet$) (Re. (9)). There is also the production of singlet oxygen ($^1O_2$) *via* the interaction between superoxide and hydroxyl radicals (Re. (10)). The presence of metal ions such as Fe^{2+} and Mn^{3+} on the surface of M100Mn activates $S_2O_8^{2-}$ to become Fe^{3+}, Mn^{4+}, and sulfate ion (SO_4^{2-}) (Re. (11) and (12)). Moreover, Fe^{3+} and Mn^{4+} are also reduced by $S_2O_8^{2-}$ to form Fe^{2+}, Mn^{3+}, and persulfate ($S_2O_8^{\bullet-}$) with weak oxidation property (Re. (13) and (14)).[57] Furthermore, Fe^{3+} and Mn^{4+} are reduced to Fe^{2+} and Mn^{3+} by photoexcited electrons (Re. (15) and (16)), which enhances the charge separation.[8,58] In addition, since the potentials of Fe^{3+}/Fe^{2+} and Mn^{4+}/Mn^{3+} redox couples are 0.77 V and 0.15 V, respectively, the reactions of Fe^{3+} and Mn^{3+} thermodynamically occurred, which boosts the internal charge transfer (Re. (17)).[59] The RhB adsorbed on the material surface would be easily oxidized by reactive oxidative species (*e.g.*, $O_2^{\bullet-}$, $^1O_2$, $SO_4^{\bullet-}$, and $HO^\bullet$) and photoexcited holes (h^+) to form mineralized products of CO_2 and water (Re. (18)).

$$\text{MIL-100(Fe)}/Mn_2O_3 + h\nu \rightarrow \text{MIL-100(Fe)}\ (e^-) + Mn_2O_3\ (h^+) \quad (6)$$

$$e^- + O_2 \rightarrow O_2^{\bullet-} \quad (7)$$

$$e^- + S_2O_8^{2-} \rightarrow SO_4^{\bullet-} + SO_4^{2-} \quad (8)$$

$$SO_4^{\bullet-} + H_2O \rightarrow SO_4^{2-} + HO^\bullet + HO^- \quad (9)$$

$$O_2^{\bullet-} + HO^\bullet \rightarrow HO^- + {}^1O_2 \quad (10)$$

$$Fe^{2+} + S_2O_8^{2-} \rightarrow Fe^{3+} + SO_4^{\bullet-} + SO_4^{2-} \quad (11)$$

$$Mn^{3+} + S_2O_8^{2-} \rightarrow Mn^{4+} + SO_4^{\bullet-} + SO_4^{2-} \quad (12)$$

$$Fe^{3+} + S_2O_8^{2-} \rightarrow Fe^{2+} + S_2O_8^{\bullet-} \quad (13)$$

$$Mn^{4+} + S_2O_8^{2-} \rightarrow Mn^{3+} + S_2O_8^{\bullet-} \quad (14)$$

$$Fe^{3+} + e^- \rightarrow Fe^{2+} \quad (15)$$

$$Mn^{4+} + e^- \rightarrow Mn^{3+} \quad (16)$$

$$Mn^{3+} + Fe^{3+} \rightarrow Mn^{4+} + Fe^{2+} \quad (17)$$

$$[h^+, O_2^{\bullet-}, {}^1O_2, SO_4^{\bullet-}, HO^\bullet] + \text{RhB} \rightarrow \text{mineralized products} + CO_2 + H_2O + SO_4^{2-} \quad (18)$$

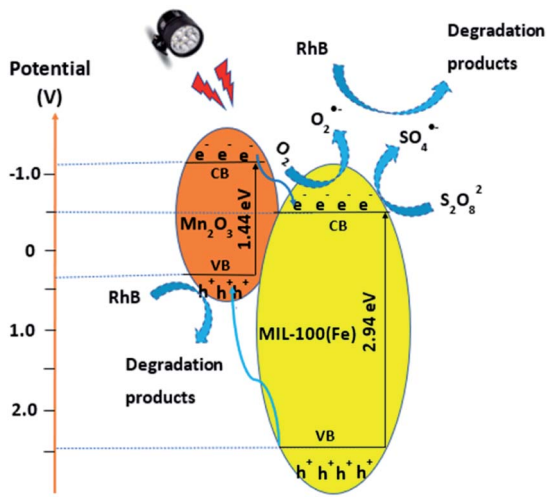

Fig. 8 The proposed mechanism for photocatalytic degradation of RhB by M100Mn(60 : 40) under visible light and persulfate activation.

Conclusions

The study was successful in the synthesis of a highly pure M100Mn composite with both advantages of highly crystalline and porous structure from Mn_2O_3 and MIL-100(Fe) for effective photocatalytic degradation of RhB in water under visible light and persulfate activation. The suitable material was found to be MIL-100(Fe)/Mn_2O_3 with a weight ratio of 60/40 and reaction conditions of pH 3, M100Mn dosage of 500 mg L^{-1}, RhB concentration of 25 mg L^{-1}, and $Na_2S_2O_8$ concentration of 300 mg L^{-1} leading to high RhB degradation of 95.91% after 90 min of the experiment. The radical quenching test showed that $HO^\bullet$, $SO_4^{\bullet-}$, $^1O_2$, $O_2^{\bullet-}$, and h^+ are all important reactive species and oxygen has a significant role in the photocatalytic reaction. A mechanism was also proposed for the oxidation of RhB catalyzed by the M100Mn composite. Besides, the stability and reusability of M100Mn were evaluated over 5 experimental cycles, proving its practicability for wastewater applications.

Conflicts of interest

There are no conflicts to declare.

Open Access Article. Published on 24 August 2021. Downloaded on 1/2/2026 2:42:14 AM.
This article is licensed under a Creative Commons Attribution-NonCommercial 3.0 Unported Licence.

Notes and references

1 B. Cuiping, X. Xianfeng, G. Wenqi, F. Dexin, X. Mo, G. Zhongxue and X. Nian, *Desalination*, 2011, **278**, 84–90.
2 E. Forgacs, T. Cserhati and G. Oros, *Environ. Int.*, 2004, **30**, 953–971.
3 J. Wu, J. Yang, G. Huang, C. Xu and B. Lin, *J. Cleaner Prod.*, 2020, **251**, 119717.
4 W. Xiao, Z. N. Garba, S. Sun, I. Lawan, L. Wang, M. Lin and Z. Yuan, *J. Cleaner Prod.*, 2020, **253**, 119989.
5 C. Huang, Y. Wang, M. Gong, W. Wang, Y. Mu and Z.-H. Hu, *Sep. Purif. Technol.*, 2020, **230**, 115877.
6 X. Li, X. Yan, X. Hu, R. Feng and M. Zhou, *J. Environ. Manage.*, 2020, **262**, 110299.
7 Y. Pang, L. Kong, D. Chen, G. Yuvaraja and S. Mehmood, *J. Hazard. Mater.*, 2020, **384**, 121447.
8 H. Heidarpour, M. Padervand, M. Soltanieh and M. Vossoughi, *Chem. Eng. Res. Des.*, 2020, **153**, 709–720.
9 J. Zhang, Z. Zhang, W. Zhu and X. Meng, *Appl. Surf. Sci.*, 2020, **502**, 144275.
10 J. Zhao, M. Ji, J. Di, Y. Zhang, M. He, H. Li and J. Xia, *J. Photochem. Photobiol., A*, 2020, **391**, 112343.
11 Y. Yang, Y. Liu, X. Fang, W. Miao, X. Chen, J. Sun, B.-J. Ni and S. Mao, *Chemosphere*, 2020, **243**, 125423.
12 K. Paździor, A. Klepacz-Smółka, S. Ledakowicz, J. Sójka-Ledakowicz, Z. Mrozińska and R. Żyłła, *Chemosphere*, 2009, **75**, 250–255.
13 G. Chen, Y. Yu, L. Liang, X. Duan, R. Li, X. Lu, B. Yan, N. Li and S. Wang, *J. Hazard. Mater.*, 2021, **408**, 124461.
14 Z. Zhou, X. Liu, K. Sun, C. Lin, J. Ma, M. He and W. Ouyang, *Chem. Eng. J.*, 2019, **372**, 836–851.
15 R. Xiao, Z. Luo, Z. Wei, S. Luo, R. Spinney, W. Yang and D. D. Dionysiou, *Curr. Opin. Chem. Eng.*, 2018, **19**, 51–58.
16 U. Ushani, X. Lu, J. Wang, Z. Zhang, J. Dai, Y. Tan, S. Wang, W. Li, C. Niu, T. Cai, N. Wang and G. Zhen, *Chem. Eng. J.*, 2020, **402**, 126232.
17 X. Zhang, H. Li, F. Hou, Y. Yang, H. Dong, N. Liu, Y. Wang and L. Cui, *Appl. Surf. Sci.*, 2017, **411**, 27–33.
18 X. Gu, J. Yue, L. Li, H. Xue, J. Yang and X. Zhao, *Electrochim. Acta*, 2015, **184**, 250–256.
19 Y. Hai, Z. Zhang, H. Liu, L. Liao, P. Fan, Y. Wu, G. Lv and L. Mei, *Front. Chem.*, 2019, **7**, 437.
20 Y. Shao, B. Ren, H. Jiang, B. Zhou, L. Liping, J. Ren, L. Dong, J. Li and Z. Liu, *J. Hazard. Mater.*, 2017, **333**, 222–231.
21 J. Zhao, Z. Zhao, N. Li, J. Nan, R. Yu and J. Du, *Chem. Eng. J.*, 2018, **353**, 805–813.
22 J. Zhao, J. Nan, Z. Zhao and N. Li, *Catal. Commun.*, 2017, **102**, 5–8.
23 J. Zhao, N. Li, R. Yu, Z. Zhao and J. Nan, *Chem. Eng. J.*, 2018, **349**, 530–538.
24 M. M. Kandy and V. G. Gaikar, *Renewable Energy*, 2019, **139**, 915–923.
25 H. Eslami, M. H. Ehrampoush, A. Esmaeili, A. A. Ebrahimi, M. H. Salmani, M. T. Ghaneian and H. Falahzadeh, *Chemosphere*, 2018, **207**, 303–312.
26 P. Horcajada, S. Surblé, C. Serre, D.-Y. Hong, Y.-K. Seo, J.-S. Chang, J.-M. Grenèche, I. Margiolaki and G. Férey, *Chem. Commun.*, 2007, 2820–2822.
27 S. Duan, J. Li, X. Liu, Y. Wang, S. Zeng, D. Shao and T. Hayat, *ACS Sustainable Chem. Eng.*, 2016, **4**, 3368–3378.
28 M. Rezaei, A. Abbasi, R. Varshochian, R. Dinarvand and M. Jeddi-Tehrani, *Artif. Cells, Nanomed., Biotechnol.*, 2018, **46**, 1390–1401.
29 X. Du, X. Yi, P. Wang, J. Deng and C.-c. Wang, *Chin. J. Catal.*, 2019, **40**, 70–79.
30 G. Chaturvedi, A. Kaur, A. Umar, M. A. Khan, H. Algarni and S. K. Kansal, *J. Solid State Chem.*, 2020, **281**, 121029.
31 D.-D. Chen, X.-H. Yi, C. Zhao, H. Fu, P. Wang and C.-C. Wang, *Chemosphere*, 2020, **245**, 125659.
32 S. Abdpour, E. Kowsari, M. R. A. Moghaddam, L. Schmolke and C. Janiak, *J. Solid State Chem.*, 2018, **266**, 54–62.
33 P. Hu, C. Chen, Y. Wang, L. Pan and C. Lu, *ChemistrySelect*, 2019, **4**, 9703–9709.
34 H. Tian, T. Araya, R. Li, Y. Fang and Y. Huang, *Appl. Catal., B*, 2019, **254**, 371–379.
35 H. Tian, J. Peng, Q. Du, X. Hui and H. He, *Dalton Trans.*, 2018, **47**, 3417–3424.
36 M.-J. Chang, W.-N. Cui, X.-J. Chai, J. Liu, K. Wang and L. Qiu, *J. Mater. Sci.: Mater. Electron.*, 2019, **30**, 1009–1016.
37 Y. Li, J. Gong, G. He and Y. Deng, *Synth. Met.*, 2011, **161**, 56–61.
38 M. Salavati-Niasari, F. Mohandes, F. Davar and K. Saberyan, *Appl. Surf. Sci.*, 2009, **256**, 1476–1480.
39 Y. Luo, B. Tan, X. Liang, S. Wang, X. Gao, Z. Zhang and Y. Fang, *Ind. Eng. Chem. Res.*, 2019, **58**, 7801–7807.
40 K. Guesh, C. A. D. Caiuby, Á. Mayoral, M. Díaz-García, I. Díaz and M. Sanchez-Sanchez, *Cryst. Growth Des.*, 2017, **17**, 1806–1813.
41 M. Y. Nassar, A. S. Amin, I. S. Ahmed and S. Abdallah, *J. Taiwan Inst. Chem. Eng.*, 2016, **64**, 79–88.
42 Y. Zhao, D.-B. Ji, P. Wang, Y.-D. Yan, Y. Xue, H.-B. Xu, Y. Liang, H.-J. Luo, M.-L. Zhang and W. Han, *Chem. Eng. J.*, 2018, **349**, 613–621.
43 M. A. Simon, E. Anggraeni, F. E. Soetaredjo, S. P. Santoso, W. Irawaty, T. C. Thanh, S. B. Hartono, M. Yuliana and S. Ismadji, *Sci. Rep.*, 2019, **9**, 1–11.
44 F. Zhang, J. Shi, Y. Jin, Y. Fu, Y. Zhong and W. Zhu, *Chem. Eng. J.*, 2015, **259**, 183–190.
45 G. Song, Z. Wang, L. Wang, G. Li, M. Huang and F. Yin, *Chin. J. Catal.*, 2014, **35**, 185–195.
46 H. Wang, R. Zhao, J. Qin, H. Hu, X. Fan, X. Cao and D. Wang, *ACS Appl. Mater. Interfaces*, 2019, **11**, 44249–44262.
47 Y. Xu, M. Lv, H. Yang, Q. Chen, X. Liu and W. Fengyu, *RSC Adv.*, 2015, **5**, 43473–43479.
48 X. Jia, R. Dai, Y. Sun, H. Song and X. Wu, *J. Mater. Sci.: Mater. Electron.*, 2016, **27**, 3791–3798.
49 Y. Zhang, J. Zhou, J. Chen, X. Feng and W. Cai, *J. Hazard. Mater.*, 2020, **392**, 122315.
50 H. Zhu, B. Yang, J. Yang, Y. Yuan and J. Zhang, *Chemosphere*, 2021, **276**, 130217.
51 S. Parvaz, M. Rabbani and R. Rahimi, *Mater. Sci. Eng., B*, 2021, **263**, 114863.

 © 2021 The Author(s). Published by the Royal Society of Chemistry

Open Access Article. Published on 24 August 2021. Downloaded on 1/2/2026 2:42:14 AM.
This article is licensed under a Creative Commons Attribution-NonCommercial 3.0 Unported Licence.

52 Y. Tian, L. Ma, X. Tian, Y. Nie, C. Yang, Y. Li, L. Lu and Z. Zhou, *Chemosphere*, 2021, **269**, 128717.
53 Y. Nosaka and A. Y. Nosaka, *Chem. Rev.*, 2017, **117**, 11302–11336.
54 B. Zhang, H. Shi, Y. Yan, C. Liu, X. Hu, E. Liu and J. Fan, *Colloids Surf., A*, 2021, **608**, 125598.
55 Y. Chen, Q. Hu, M. Yu, X. Gong, S. Li, S. Wang, H. Yu and Z. Li, *CrystEngComm*, 2021, **23**, 5070–5077.
56 P. Hu, C. Chen, Y. Wang, L. Pan and C. Lu, *ChemistrySelect*, 2019, **4**, 9703–9709.
57 J. Li, R. Guo, Q. Ma, L.-c. Nengzi and X. Cheng, *Sep. Purif. Technol.*, 2019, **227**, 115669.
58 Y. Liu, H. Guo, Y. Zhang, X. Cheng, P. Zhou, G. Zhang, J. Wang, P. Tang, T. Ke and W. Li, *Sep. Purif. Technol.*, 2018, **192**, 88–98.
59 Z. Dong, Q. Zhang, B.-Y. Chen and J. Hong, *Chem. Eng. J.*, 2019, **357**, 337–347.
60 K.-Y. Andrew Lin, H.-A. Chang and C.-J. Hsu, *RSC Adv.*, 2015, **5**, 32520–32530.
61 S. Miao, Z. Zha, Y. Li, X. Geng, J. Yang, J. Yang and S. Cui, *J. Photochem. Photobiol., A*, 2019, **380**, 111862.
62 C. Yang, G. Zhang, Y. Meng, G. Pan, Z. Ni and S. Xia, *J. Hazard. Mater.*, 2021, **408**, 124908.
63 M. Sabri, A. Habibi-Yangjeh, H. Chand and V. Krishnan, *Sep. Purif. Technol.*, 2020, **250**, 117268.
64 M. Sabri, A. Habibi-Yangjeh and S. Vadivel, *J. Mater. Sci.: Mater. Electron.*, 2019, **30**, 12510–12522.
65 M. Sabri, A. Habibi-Yangjeh and S. Ghosh, *J. Photochem. Photobiol., A*, 2020, **391**, 112397.
66 B. Zhu, H. Cheng, J. Ma, Y. Kong and S. Komarneni, *Chemosphere*, 2019, **237**, 124547.